Geochemistry, Geophysics, Geosystems®

Key Points:

- Laser ablation inductively coupled plasma mass spectrometry imaging investigates the geochemical composition and localization of particles in samples of the East Greenland Ice Core Project ice core, East Greenland
- The maps reveal clusters of insoluble particles 50–60 times larger than an average particle, at intra-grain locations and grain boundaries
- Geochemical signals of the particles are consistent with cryo-Raman spectroscopy and with known dust sources and sea salt aerosol

Supporting Information:

Supporting Information may be found in the online version of this article.

Correspondence to:

P. Bohleber,
pascal.bohleber@unive.it

Geochemical Characterization of Insoluble Particle Clusters in Ice Cores Using Two-Dimensional Impurity Imaging

Pascal Bohleber[1] , Nicolas Stoll[2,3] , Martin Rittner[4], Marco Roman[1] , Ilka Weikusat[2,5], and Carlo Barbante[1,6]

[1]Department of Environmental Sciences, Informatics and Statistics, Università Ca' Foscari, Venice, Italy, [2]Alfred Wegener Institute Helmholtz Center for Polar and Marine Research, Bremerhaven, Germany, [3]Department of Geosciences, University of Bremen, Bremen, Germany, [4]TOFWERK AG, Thun, Switzerland, [5]Department of Geosciences, Eberhard Karls University of Tübingen, Tübingen, Germany, [6]Institute of Polar Sciences, CNR, Venice, Italy

Abstract Understanding post-depositional processes altering the layer sequence in ice cores is especially needed to avoid misinterpretation of the oldest and most highly thinned layers. The record of soluble and insoluble impurities represents an important part of the paleoclimate proxies in ice cores but is known to be affected through interaction with the ice matrix, diffusion, and chemical reactions. Laser ablation inductively coupled plasma mass spectrometry (LA-ICP-MS) has been recognized for its micron-scale resolution and micro-destructiveness in ice core impurity analysis. Employing LA-ICP-MS for 2D chemical imaging has already revealed a close relationship between the ice grain boundary network and impurity signals with a significant soluble component, such as Na and Mg. Here we show the latest improvements in chemical imaging with LA-ICP-MS, by increasing the spatial resolution to 20 µm and extending the simultaneous analysis to also mostly insoluble impurities, such as Al and Fe. All analytes reveal signals of dispersed spots in a sample of an East Greenland ice core. Based on their average size around 50–60 times larger than an average particle and their heterogeneous elemental ratios these spots are interpreted as particle clusters. To distinguish their origin, a simple colocalization classification reveals elemental ratios consistent with marine and mineral dust aerosol. Based on already existing data from cryo-Raman spectroscopy, we discuss potential ways to integrate the two methods in a future comparison. Such a combined approach may help constraining post-depositional changes to the dust-related insoluble impurity components, such as cluster formation and chemical reactions at grain boundaries.

Plain Language Summary Aerosols of marine and terrestrial origin delivered to the polar ice sheets are archived in the ice and can be studied via the analysis of ice cores. The chemical composition and size of mineral dust can deliver important information about past climatic changes and atmospheric transport. However, it has already been shown that this insoluble material is not always passively archived in the ice but can undergo changes in its chemical composition and size, for example, by forming particle aggregates. To investigate these processes, it is preferable to study the chemical composition of insoluble particles and their localization within the ice matrix. Here we show how this can be done by a new chemical imaging method for ice using laser ablation inductively coupled plasma mass spectrometry. In a sample of a Greenland ice core we find clear signals of particle clusters, 50–60 times larger than a single particle. Based on their chemical composition, it is possible to differentiate between marine and terrestrial material. We discuss the results against findings previously obtained for the same sample from a different method, cryo-Raman spectroscopy. Bringing together several methods may provide important added value for a more comprehensive understanding of these important indicators of past climate.

1. Introduction

Polar ice cores are an invaluable archive of past climate, thanks to recording a unique variety of proxies such as greenhouse gas concentrations and aerosol-related atmospheric impurity records over time-scales from decades up to hundreds of millennia (e.g., Fischer et al., 2021). The investigation of the deepest and highly thinned ice core layers remains a fundamental frontier in ice core research, being the key to unlock the oldest parts of the ice core record. As a new 1.5 million year-old ice record may soon be recovered from Antarctica (Brook et al., 2006; Fischer et al., 2013), it is also an increasingly pressing challenge. Given that each meter of such an "Oldest" ice core section expected around 2,500 m depth at Little Dome C may comprise more than 10,000 years (Lilien

et al., 2021), we face the need for innovative high-resolution analysis. However, especially important for deep ice, it is equally important to carefully assess the integrity of the climate proxy signals in order to avoid misinterpretation (Faria et al., 2010). This is a particular challenge for the ice impurity records, which can interact with the ice crystal matrix through several processes. As ice grains grow in size, especially in deep ice, they can either displace impurities which are subsequently preferentially located at the grain boundaries, or experience drag by inclusions of insoluble impurities (Stoll, Eichler, Hörhold, Shigeyama, & Weikusat, 2021 and references within). On the one hand, especially soluble species are affected by the diffusion along the network of ice veins, which can cause possible post-depositional alteration of ice core paleoclimate records (Ng, 2021; Rempel et al., 2001). On the other hand, post-depositional change has also been documented for insoluble impurities related to dust deposition. This concerns not only systematic changes in their size distribution by forming of aggregates (Lambert et al., 2008). Recently it was shown that englacial chemical reactions between dust particles and acidic environments formed within grain boundaries can result in post-depositional alteration of their geochemical signature (Baccolo et al., 2021). Both size distribution and geochemical composition are valuable indicators of past atmospheric transport and dust sources (Albani et al., 2012; Baccolo et al., 2018). Taking into account the localization of insoluble particles within the ice grain matrix will be fundamental for detecting and constraining post-depositional changes to dust-related ice core proxies, ultimately leading to their improved interpretation in the deep parts of existing and future ice cores.

In this framework, ice core impurity analysis with laser ablation inductively coupled plasma mass spectrometry (LA-ICP-MS) has great potential due to its micron-resolution and micro-destructiveness (Müller et al., 2011; Sneed et al., 2015). LA-ICP-MS has recently been refined for two-dimensional high-resolution impurity imaging of ice cores (Bohleber et al., 2020). This new approach revealed a high degree of localization at grain boundaries of mostly soluble chemical species such as Na, but also clear differences among ice from glacial and interglacial periods (Bohleber, Roman, Šala, et al., 2021). As a result of these developments, LA-ICP-MS chemical imaging has become an important additional technique for investigating the localization of impurities in the ice matrix, supplementing methods such as energy-dispersive X-ray spectroscopy (e.g., Barnes et al., 2003), X-ray spectroscopy coupled with scanning electron microscopy (e.g., Barnes & Wolff, 2004), and cryo-Raman microscopy (e.g., Eichler et al., 2017). A combination of such methods promises to shed light on existing discrepancies, cross-validate different instrumental techniques and to eventually reveal a more holistic picture on the location of impurities in ice. Such a view may provide an improved understanding not only of the paleoclimatic record related to chemical impurities, but also of their impact on the dielectric and deformational ice properties (Stoll, Eichler, Hörhold, Shigeyama, & Weikusat, 2021).

Refining further our previous work on 2D chemical imaging on ice cores with LA-ICP-MS (Bohleber et al., 2020), we have increased the spatial resolution from 35 to 20 μm and extended the analysis to new elements such as Al and Fe, mostly associated to insoluble impurities. A carefully selected sample of a Greenland ice core, previously analyzed by cryo-Raman spectroscopy (Stoll, Eichler, Hörhold, Erhardt, et al., 2021; Stoll et al., 2022) was analyzed in order to test the refined approach with LA-ICP-MS chemical imaging. We show here how image analysis helps to separate the signals of grain boundaries and clusters of insoluble particles, laying the ground for investigating the geochemical signature of insoluble material in the ice with LA-ICP-MS, also in concert with other methods.

2. Materials and Methods

2.1. Sample Selection

For the purpose of this study, a sample of the East Greenland Ice Core Project (EGRIP) ice core was selected, named S10 in the study by Stoll et al. (2022). This selection aimed at (a) choosing a sample with considerable quantities of insoluble particles and (b) exploiting the synergy with recently conducted cryo-Raman spectroscopy analyzed on the same sample. S10 is from about 1,256.95 m depth, corresponding to the Younger Dryas period and showing distinctly elevated levels of insoluble particles in meltwater analysis, ranging from about 1 to $2.5 \cdot 10^5$ particles/ml (Figure 2 in Stoll et al., 2022). In addition, S10 contains a so-called "cloudy band," visible layers rich in impurities resulting from seasonal events like atmospheric storms (Svensson et al., 2005). S10 thus samples a horizontal layer of much higher dust content than the area above and below. Further details of the cryo-Raman analysis conducted on the EGRIP ice samples and their chemical characterization can be found in Stoll et al. (2022).

2.2. Refining Chemical Ice Core Imaging With LA-ICP-MS for Insoluble Particle Detection

The LA-ICP-MS setup at the University of Venice comprises an Analyte Excite ArF excimer 193 nm laser (Teledyne CETAC Photon Machines) with a HelEx II two-volume ablation chamber. Using a rapid aerosol transfer line, the ablated material is transported to an iCAP-RQ quadrupole ICP-MS (Thermo Scientific) for elemental analysis. A custom-built cryogenic sample holder keeps the ice core samples below their freezing point. The circulation of a glycol–water mixture cooled to −35°C keeps the surface temperature of the ice samples consistently at −23°C ± 2°C. Details on the developed ice core 2D chemical imaging have already been presented elsewhere (Bohleber et al., 2020). Here we describe the latest adaptions in the framework of analyzing the EGRIP samples, with special focus on detecting insoluble particles. Following cryo-Raman spectroscopic analysis at the Alfred Wegener Institute, Helmholtz Centre for Polar and Marine Research, Germany, the samples were transported via a commercial freezer transport to the University of Venice and did not show any indications of alteration or melting.

The entire sample surface (10.45 × 48.50 mm, Stoll et al., 2022) was decontaminated by manual scraping using a ceramic ZrO_2 blade (American Cutting Edge, USA). Once the sample is inside the ablation chamber, a mosaic of optical images of the ice sample surface is obtained using the integrated camera. The mosaic optical images show entrapped air bubbles (dark circles) and individual ice crystals and their boundaries (dark lines). Comparing the optical images with the LA-ICP-MS chemical images permits to investigate the localization of impurities within the ice crystal matrix.

Before each image acquisition, the surface is further decontaminated by at least one pre-ablation run using an 80 × 80 μm square spot. Chemical imaging is performed as a raster scan with a square spot without overlap perpendicular to the scan direction, and without any post-acquisition spatial interpolation. One scan line on the synthetic glass NIST SRM 612 is measured before and after the acquisition of each image, respectively. The resulting chemical images are from now on only addressed as (elemental) maps in order to distinguish them from the optical image mosaics, if not noted otherwise. In the experimental design employed in this study, initial 35 μm resolution maps were used to select sub-regions for additional imaging at 20 μm resolution. Background and drift correction as well as image construction are performed using the software HDIP (Teledyne CETAC Photon Machines).

In comparison to the previously analyzed Antarctic ice core samples (Bohleber, Roman, Šala, et al., 2021), the higher impurity content of the EGRIP S10 sample allowed us to add further analytes to the previous used three to four chemical channels per elemental map (mainly ^{23}Na, ^{24}Mg, and ^{88}Sr). Analytes with predominant insoluble components in the ice were selected, with special focus on ^{27}Al but including also the exploration of ^{29}Si, ^{43}Ca, and ^{56}Fe. Details on the data acquisition parameters are summarized in Table S1 in Supporting Information S1. The dwell times of the different analytes were carefully distributed to optimize signal-to-noise ratios in the maps. In addition to investigating the co-localization of elements based on their spatial intensity distribution, elemental (mass) ratios were calculated for quantitative analysis. The NIST SRM 612 was used as a reference material (Jochum et al., 2011; Longerich et al., 1996), following a previously employed approach (Bohleber, Roman, Šala, et al., 2021; Della Lunga et al., 2014).

3. Results
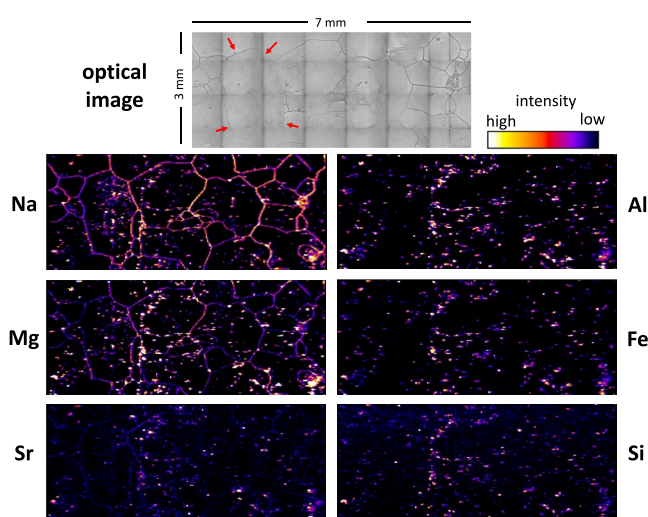
3.1. Basic Image Characteristics

The elemental maps show the same basic image characteristics already found in Antarctic ice (Bohleber, Roman, Šala, et al., 2021), but the higher resolution of 20 μm enables novel, more detailed insights. We found high intensities tracking the grain boundaries and dispersed bright spots in the grain interiors. At 35 μm resolution, it is generally not possible to clearly distinguish these bright spot features in the grain interiors (Figure S1 in Supporting Information S1). Accordingly, we focus here on three maps recorded with a 20 μm spot over adjacent areas of 3 × 7 mm each. The maps were obtained in a region showing visible evidence for the cloudy band and intersecting an area previously investigated by Stoll et al. (2022) using cryo-Raman analysis (Figure 1). In the following these maps are named "Area 1, 2, and 3" (A1, A2, and A3), respectively. The optical image recorded during microstructure mapping or prior to the Raman spectroscopy analysis shows a visible slightly darker layer running quasi-horizontally through the image, marking the cloudy band. It is also possible to recognize an ice
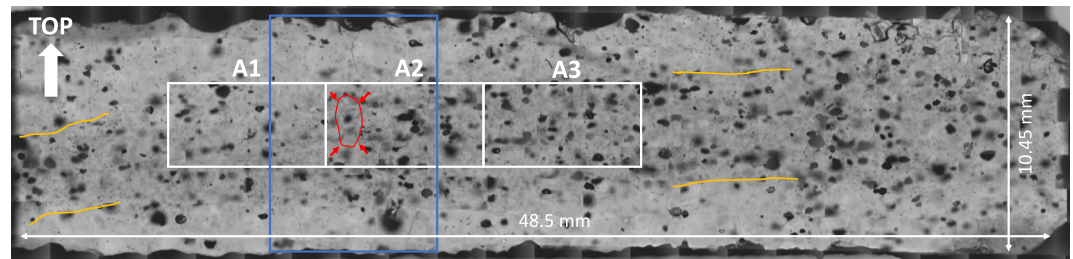
Figure 1. Microstructure mapping mosaic of optical images recorded prior to cryo-Raman analysis. The locations of the three areas analyzed by laser ablation inductively coupled plasma mass spectrometry at 20 μm resolution are indicated as white boxes (A1–A3). The location of the cryo-Raman analysis of S10 in Stoll et al. (2022) is shown as a blue box for reference. The cloudy band is visible as a slightly darker band running quasi-horizontally through the sample. For better visibility, approximate boundaries of the cloudy band are indicated by yellow lines. Red arrows point to an ice grain that stands out by its elongated vertical shape (outlines traced in red) and thus can be used as a reference to the elemental map A2. Note that this is a small slice of an ice core and the arrow "TOP" points toward the top of the core (i.e., the surface).

grain standing out by its elongated vertical (to the core axis) shape, which was also recognizable in the optical images recorded with the LA-ICP-MS setup, albeit a fresh surface was prepared by scraping.

Figure 2 shows an example for the maps obtained at 20 μm resolution by LA-ICP-MS for Area 2. Areas 1 and 3 show the same basic characteristics and are shown in Figures S2 and S3 in Supporting Information S1. Grain boundaries and a few air bubbles are recognizable in the optical image. The maps of Na and, to a lesser extent also Mg and Sr, generally show high intensities at the locations of grain boundaries. This grain boundary association is lacking for the other elements, however. All chemical channels show dispersed bright spots in grain interiors and occasionally at grain boundaries. Albeit no collision-reaction gas was used in the ICP-MS analysis to reduce spectral interferences, Fe shows a good signal-to-noise ratio, with clearly recognizable bright spots generally co-localized with Al. In the background corrected signal, Al and Fe typically have signals of a few 10,000 counts above background, and Si still a few 1,000. The signal to noise contrast was found to be much lower for Ca, typically a few 10–100 counts. Accordingly, Ca is not considered further in the following.

3.2. Simple Co-Localization Analysis

For a simple colocalization analysis, Spearman's rank correlation coefficient (SRC) is calculated among the chemical elements after combining all datasets of maps A1, A2, and A3 and taking the logarithm (base 10) of the intensities. The respective correlation matrix is nearly identical for Pearson's correlation coefficient (Figure S4 in Supporting Information S1). The correlation matrix shows that Na and Mg are highly correlated. Al, Fe, and Sr feature substantial correlation, in particular Al and Fe, and Sr showing good correlation additionally with Mg. The correlation coefficient is a simple metric, however, and applying it to the entire data sets can only serve as a first indication, not least because it disregards important details regarding the relative spatial distribution among the elements (Bohleber, Roman, Šala, et al., 2021). This becomes evident in elemental maps with separate color channels for individual elements, providing an improved visual colocalization analysis. For example, Figure 4 shows that Al, Si, Fe appear frequently together but occasionally also individually: the maps reveal some isolated areas of green and blue pixels, that is, populated dominantly only by Fe or Si, respectively. This occasional isolated occurrence of Si is especially relevant considering the lower correlation values found for Si.

Figure 2. Laser ablation inductively coupled plasma mass spectrometry elemental maps of Area 2 (3 × 7 mm) combined with a mosaic of optical images of the ice surface in the ablation chamber (top). Na and Mg show high intensities tracking the grain boundary network. All elements show dispersed bright spots at grain boundaries and in grain interiors. Red arrows in the optical image mark the same ice grain as in Figure 1 for reference.

3.3. Image Segmentation and Chemical Classification

In order to proceed from visual analysis to a more quantitative evaluation, it is key to isolate the pixels in a map that are related to a specific physical

feature, such as the grain boundaries or dispersed spots as possible indicators of insoluble particles. This extraction of patterns from an image is referred to here as image segmentation. With a watershed algorithm, for example, by using an integrated function of the imaging processing within the software HDIP, it is possible to detect the grain boundary network in the Na maps (Bohleber, Roman, Šala, et al., 2021). In order to separate the pixel locations of the dispersed spots we considered the Al channel since it is showing the clearest signal for these features and generally has little or no association with the grain boundary network. We applied thresholding at the 90th percentile followed by binarization to isolate a mask for the dispersed spots. Notably, this simple division of image features into grain boundaries and dispersed spots already explains the bimodal distribution seen in most elemental ratios. Figure 5 gives an example for the Mg/Al ratio of Area 2, showing two different modes in the distribution. Due to the relative lower Al intensity at grain boundaries, the respective values of Mg/Al are higher than the values detected for the bright spots. The opposite is seen for ratios involving Na as the denominator.

Combining the thresholding masks for two or more channels and simple logical operators, it is possible to refine the segmentation procedure into a simple classification scheme, for instance to detect "Fe and Al," "Si without Al," etc. A particular interesting class in this regard is "Na with Mg but without Al," which can indicate the locations dominated by marine aerosol. Figure 6 provides an illustration of this image segmentation and classification. Table 1 shows the median of elemental mass ratios obtained for selected pairs of elements, targeting specifically those ratios relevant for characterizing the dispersed spots for further comparison against references from other studies. These ratios were obtained after thresholding of each component, using the 90% percentile. This choice of threshold served to exclude the second mode in the distribution associated with the grain boundaries (cf. the orange distribution in Figure 5), while still resulting in a substantial number of pixels being considered (typically between 2,500 and 3,500). Unless the threshold value resulted in including part of the second mode, the choice of threshold value did not result in major differences in the obtained elemental ratios. As a measure for the spatial variability in the average ratios, Table 1 includes the range in median values obtained from the three different maps. This results in a relative variability of consistently around 30%.

4. Discussion

4.1. Interpreting Dispersed Bright Spots as Clusters of Insoluble Particles

Given that the mean diameter of individual dust particles was estimated to be around 1.5 μm in the NGRIP Greenland ice core from the Younger Dryas (Ruth et al., 2003), it is worth noting that the dispersed spots in the maps dominantly occur in clusters of several pixels, hence being larger than a few 20 μm. The area of these clusters can be calculated, by summing up the respective number of pixels. Translating the average of the cluster area into a circular-equivalent diameter results in 80–90 microns. As a tentative approximation, this would mean that the clusters consist typically of 50–60 individual particles, although particles as large as 10 μm were also detected by Ruth et al. (2003). If using the simple marker Al for material likely of terrestrial origin for detecting particle locations in the map, the resulting correlation matrix shows not only increased correlation values among the likely dust-related Al, Si, Fe but also significant correlation between Na, Mg, and Si (Figure 3b). This indicates the co-presence of various elements in the clusters segmented by Al-thresholding. The elemental ratios inside the clusters show indeed a high degree of variability (Figure 7). In the light of these results, it becomes clear that the dispersed bright spots cannot be regarded as single homogeneous objects but are representing clusters of insoluble particles of various origin, similar to observations by Stoll, Eichler, Hörhold, Erhardt, et al. (2021) and Stoll et al. (2022). Similar properties were observed for clusters of black carbon and dust in shallow parts of Antarctic ice cores (Ellis et al., 2016). Because of the heterogeneity of the clusters, calculating elemental ratios on the pixel-level with pairwise thresholding is more adequate than to calculate elemental ratios for entire clusters. A notable result in this regard comes from the class "Mg with Na without Al," defined to represent material of marine origin following previous classifications (Oyabu et al., 2020). As shown in Figure 6d), this classification results frequently in selecting entire particle clusters, in particular inside the vertically elongated grain previously noted for Area 2, but also inside other grains. The elemental ratios obtained following this classification substantiate the association with a marine origin: The Mg/Na elemental mass ratio of 0.03–0.04 deviates from the ratio of 0.12 of bulk seawater. While a non-sea-salt related contribution could remain from the heterogeneous particle aggregates (Figure 7), it also has to be noted that considerable scatter in the Mg/Na values of sea salt particles can occur due to fractionary recrystallization in aerosol formation (Mouri et al., 1993). The range observed here is consistent with ratios obtained for sea salt aerosol particles larger or equal than 2 μm in diameter (Mouri

a)

b)
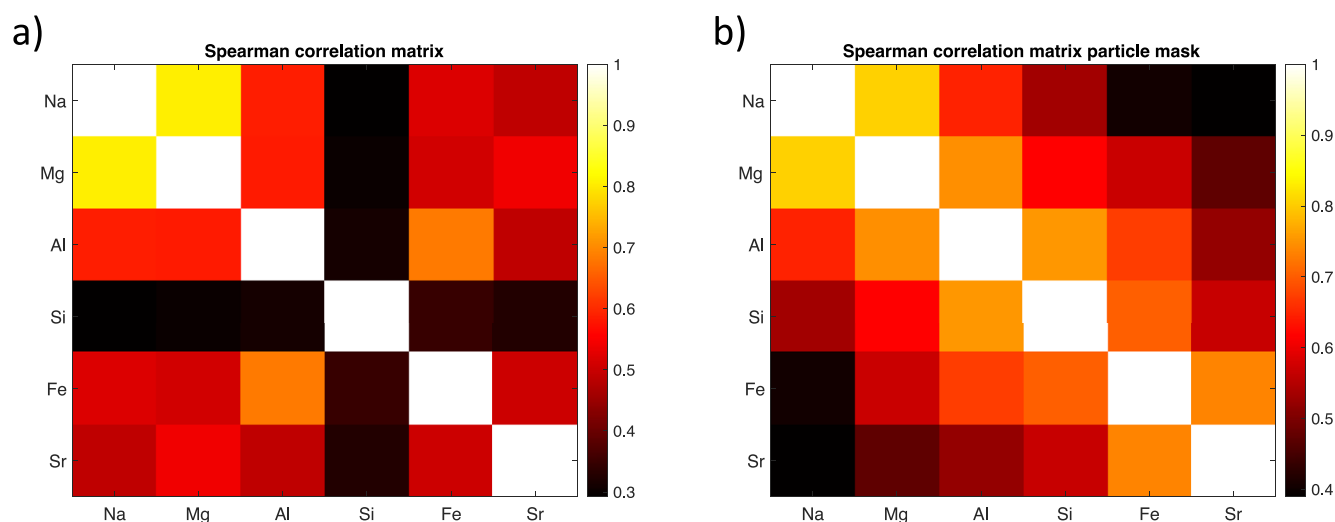
Figure 3. Correlation matrix showing the Spearman's correlation coefficient among all chemical elements for the logarithmic intensities obtained from the combined maps A1, A2, and A3 (a). Shown in panel (b) are the correlations after segmentation of the bright spot image features via thresholding of the Al channel (see text).

et al., 1993). The elemental ratios shown in Table 1 for pairs of Mg, Al, Si, and Fe are close to values reported for bulk measurements of Asian desert samples (Formenti et al., 2011; Jeong, 2008) and thus substantiate the interpretation as being of mineral dust origin. In particular regarding the Mg/Al and Fe/Al ratios, the results are also consistent with the range of values obtained from EGRIP samples analyzed by continuous flow analysis (CFA) coupled to a time-of-flight (TOF) mass spectrometer (Erhardt et al., 2019), albeit lower than the average reported there. Given that the CFA data set represents the analysis of meltwater of several meters of ice core, a comparison with the present data set representative of a few square mm at a fixed depth is not directly feasible. A comparison between LA-ICP-MS and CFA data sets has provided valuable insights in the past for line profiles measured by LA-ICP-MS along the main core axis (Bohleber et al., 2018; Della Lunga et al., 2017; Spaulding et al., 2017). In this view, a future comparison with the traditionally employed dust and dust size characterization in meltwater analysis seems promising, especially if enhanced by the quasi-simultaneous TOF single particle detection. LA-ICP-MS avoids acidification of the sample, and an inter-method comparison may shed light on the fate of the particle clusters detected in the analysis of solid ice samples when measured in meltwater.

4.2. Toward Bridging the Method Gap for Future Comparison With Cryo-Raman Analysis

Combining data sets obtained from complementary methods can provide a more complete characterization of the ice core glaciochemisty (Stoll, Eichler, Hörhold, Shigeyama, & Weikusat, 2021). So far, the comparatively recent LA-ICP-MS chemical imaging technique has not been integrated, neither into inter-laboratory comparisons nor in an inter-method comparison study. In particular for the comparison with cryo-Raman spectroscopy, the refined approach presented here may help to bridge the method gap. Although awaiting still a full exploitation, a few promising directions are already becoming evident from the results presented here.

4.2.1. Impurity Localization in the Ice Matrix

It is now possible to extract the locations of insoluble material in the elemental maps and to compare this with information on the spatial distribution determined by microstructure mapping and cryo-Raman analysis. Qualitatively, it is possible to compare if the same regions in a sample are populated by insoluble particles. Furthermore, Raman data enables a more efficient way to choose promising analytes for LA-ICP-MS. On a semi-quantitative level, it can be determined what relative percentage of insoluble particles are located at or in close vicinity to grain boundaries. Figure 8 provides a first (imperfect) example of such a classification attempt: After segmenting the grain boundary network via the Na channel and the particle locations via Al, it is determined which pixels are in overlap between the two. In the map shown in Figure 8, about 41% of the pixels belonging to the Al class are at a location that also belongs to the grain boundary class. If counting groups of connected pixels as a single object, a similar ratio is obtained: About 43% of the objects overlap with grain boundaries. This is
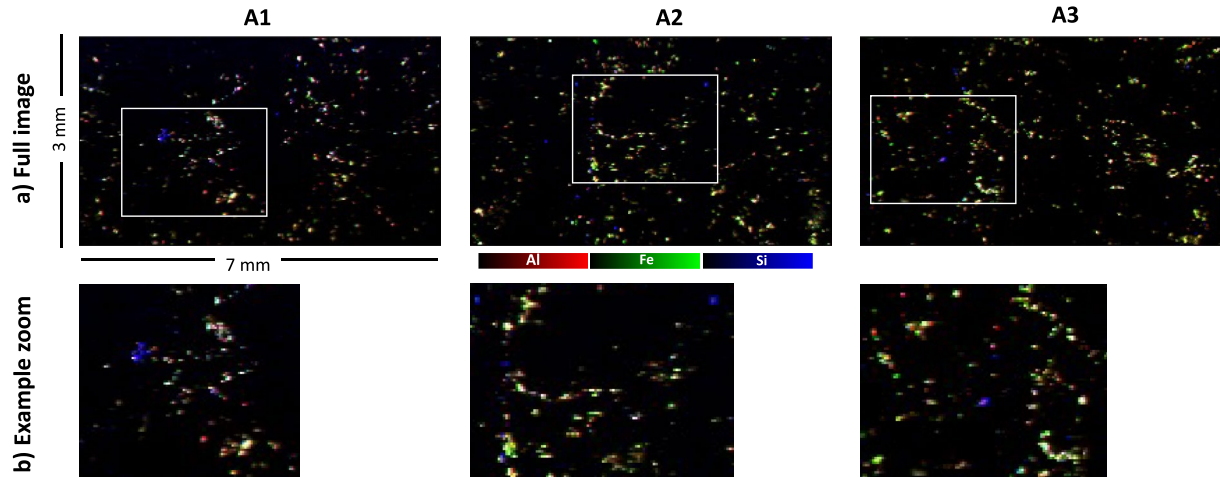
Figure 4. Visual colocalization analysis between Al, Fe, and Si for the three areas, with their intensities shown in red, green, and blue, respectively. Colocalization between Al and Fe are abundant (yellow) and also frequently found for all three elements (white). Occasionally, Si also occurs individually (blue spots). The top row shows (a) the full elemental maps and (b) the bottom row provides an example zoom-in for the areas marked by white rectangles in panel (a).

only minimally higher than the typical 22%–42% of visible inclusions detected at grain boundaries in the EGRIP samples (Table 2 in Stoll, Eichler, Hörhold, Erhardt, et al., 2021). Unfortunately, during the cryo-Raman analysis of sample S10 no detailed analysis of the localization at grain boundaries was conducted due to the large number of micro-particles present. However, the sample from a depth of 1,339.75 m has a comparable count of insoluble particles as in S10, and showed 42.4% of micro-inclusions located close to grain boundaries (Stoll, Eichler, Hörhold, Erhardt, et al., 2021), a similar percentage to what is found here for S10. The method based on LA-ICP-MS imaging presented here is thus a valuable addition to established visual approaches of investigating the relationship between solid inclusions and grain boundaries by overcoming methodological limitations. This particularly concerns the fact that the number and localization of particle clusters (e.g., at grain boundaries) can be determined semi-automatically, as opposed a manual counting technique employed in visual analysis.
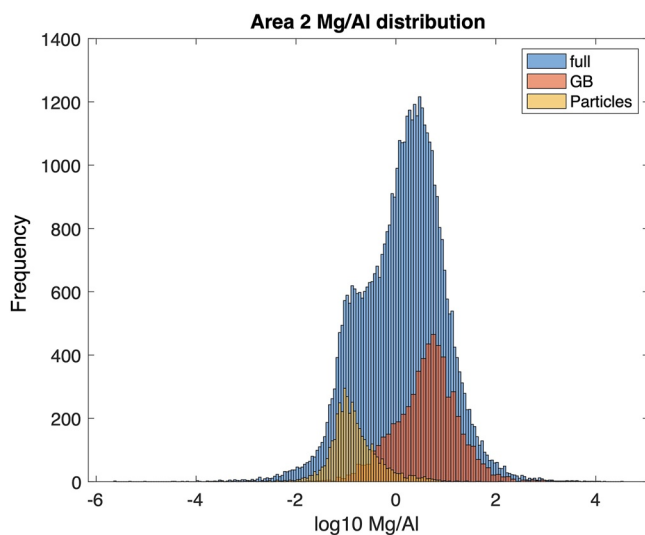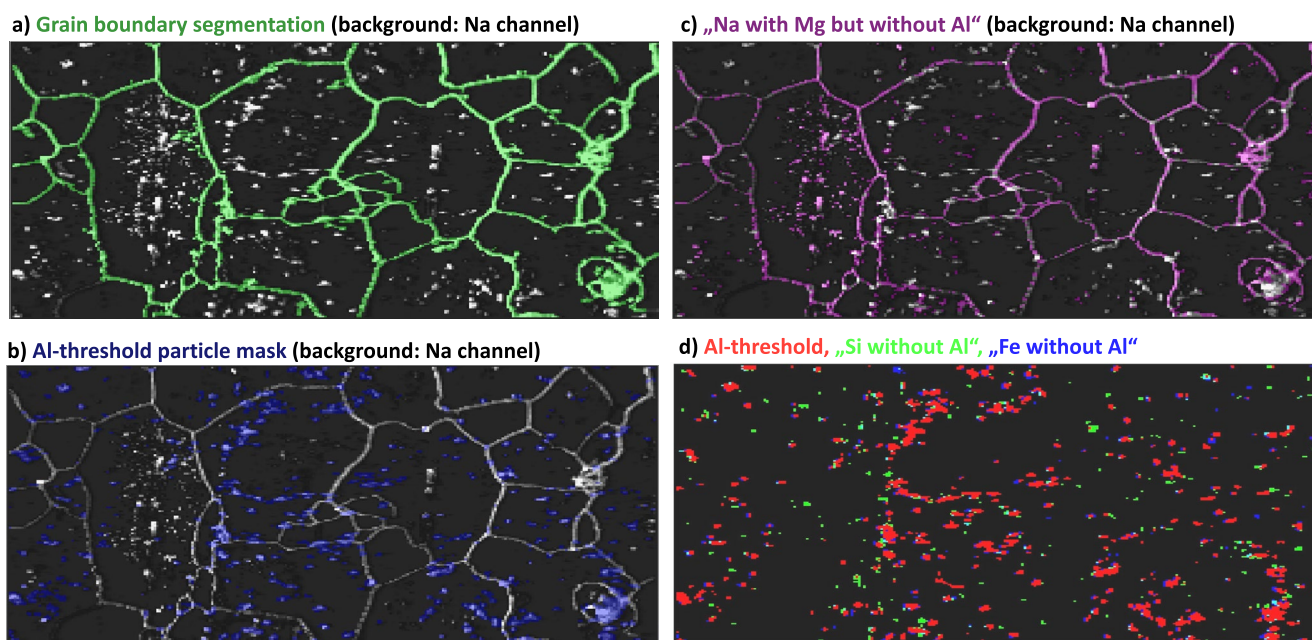

Figure 5. Example distribution of Mg/Al for Area 2. Note the two distinct modes in the values obtained for the entire map ("full"), which can be associated with the grain boundaries ("GB") and the dispersed bright spots ("Particles"). The distributions for grain boundaries and bright spots were obtained from separate data sets after segmentation (see text).

Some areas can be erroneously classified as grain boundaries, the segmented image in Figure 8 likely systematically overestimates the relative fraction of particles at grain boundaries. The optical image mosaics offer an alternative for grain boundary segmentation, but at presented this is still hampered by insufficient image quality. In addition, more powerful techniques for image segmentation exist, for example, based on deep learning approaches (Khanal & Estrada, 2020). Like many other tools of modern computer vision, this may provide important assistance to evaluating the complex information comprised in the elemental maps in the near future (Bohleber, Roman, Barbante, et al., 2021).

4.2.2. Geochemical Signature of Particle Clusters

When aiming at a semi-quantitative comparison of the glaciochemical particle characterization, additional challenges arise due to the differences in the analytical methods: While LA-ICP-MS determines the total amount (soluble and insoluble) for each element, cryo-Raman spectroscopy detects the spectra of individual minerals. An unambiguous detection of minerals based on the co-localization of elements in the maps is not straightforward, because the elemental ratios employed here are not fully selective indicators: Minerals can contain an (unknown) contribution from different elements, for example, various sulfates, or either Al or Si being present in feldspar (Table A1 in Stoll et al., 2022). Moreover, as shown above, the particle clusters comprise a heterogeneous mix of minerals while retrieving a clear mineralogy-dependent localization is still challenging (Stoll et al., 2022). A statistical approach to

a) Grain boundary segmentation (background: Na channel)

b) Al-threshold particle mask (background: Na channel)

c) „Na with Mg but without Al" (background: Na channel)

d) Al-threshold, „Si without Al", „Fe without Al"

Figure 6. Illustration of the image segmentation and classification masks employed, using Area 2 as an example. Panel (a) shows the grain boundary segmentation using a watershed algorithm (HDIP) in green, with the Na channel shown in white as background. Panel (b) shows the particle mask obtained from thresholding of the Al channel (in blue, Na channel white in background). Panel (c) shows the classification of "Na with Mg but without Al" (in pink, illustrated on top of the Na map, unselected pixels white in background). Panel (d) shows the Al threshold in red together with "Si without Al" and "Fe without Al" in green and blue, respectively.

comparing the average composition thus appears more adequate. A promising link in this regard are classifications such as "Si without Al" and "Fe without Al." The former is consistent with the occurrence of quartz minerals (SiO_2) while the latter indicates minerals such as hematite (Fe_2O_3) or jacobsite ($MnFe_2O_4$). Jacobsite could be distinguished by measuring Mn, which has been detected previously with LA-ICP-MS imaging (Bohleber et al., 2020). Determining the relative fraction of pixels showing Si or Fe only versus pixels showing either Al or Si (or Fe, respectively) offers a tentative indicator or the relative abundance of these minerals according to the LA-ICP-MS maps, which can be compared to the previous findings by cryo-Raman analysis. In contrast to the averaged elemental ratios, the number of pixels determined by this procedure is found to be more sensitive to thresholding, however. As a first indication, the threshold was adapted to 95th percentiles in order to suppress counting of spurious single pixels. This reveals a relative abundance of "Si without Al" of 28%, 22%, and 20% for A1, A2, and A3, respectively. This is close to the about 20% of quartz found in the same sample by cryo-Raman analysis (Stoll et al., 2022). For "Fe without Al" the results are consistently 21% for A1, A2, and A3, respectively, which is higher than the result of Stoll et al. (2022), however, who found only about 6% of hematite in this sample.

A particular interesting result in the cryo-Raman investigation was the comparatively high amount of dolomite ($CaMg(CO_3)_2$) found in the sample S10. Although a clear Ca signal was not obtained for the maps, Sr can provide a tentative indicator in this context, since it has also been observed both in gypsum and dolomite (Playà & Rosell, 2005; Sánchez-Román et al., 2011). In a visual colocalization analysis (Figure S5 in Supporting Information S1), Sr occurs occasionally on its own. Using the classification "Sr without Mg and without Al" and "Sr with Mg but without Al" as tentative indicators for gypsum and dolomite, respectively, reveals a comparatively larger presence of the gypsum versus the dolomite class: Taking pixels that have either Al or Sr (after 95% thresholding) as a reference gives 25%, 28%, and 27% for the relative abundance of "Sr without Mg and without Al." For "Sr with Mg but without Al" this is reduced to 8%, 7%, and 4%, respectively. In view of these results, showing some agreement but also some discrepancies, it seems worth noting that apart from the methodological challenges, one also has to consider spatial variability. Although only a sub-selection of all detected particles was identified

Table 1
Average Elemental Mass Ratios Extracted After Thresholding for Two-Elemental Co-Localization (See Text)

|	Mg/Na (no Al)	Mg/Al	Mg/Fe	Si/Al	Fe/Al
EGRIP S10	0.03–0.04	0.10–0.13	0.39–0.52	4.1–5.5	0.26–0.32
UCC	0.46	0.17	0.38	3.83	0.44

Note. The range refers to the spread in median values obtained among the three maps. Reference values for the upper continental crust (UCC) are from McLennan (2001).
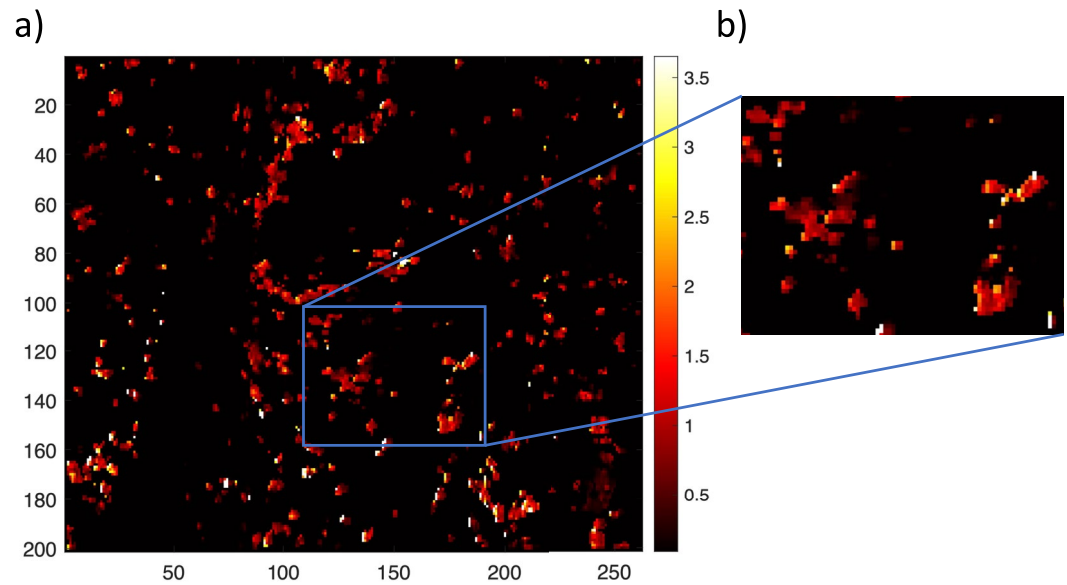
Figure 7. The Al/Na elemental mass ratio for locations determined by Al thresholding in Area 2 (see text). Panel (a) shows the full map with a zoom-in to blue square shown in panel (b). Note that the particle clusters generally show a large degree of heterogeneity in their elemental ratios, indicating a heterogeneous composition.

in their mineralogy in the cryo-Raman study, substantial amount of spatial heterogeneity is typically seen in the EGRIP samples. Although A1 and A2 partially overlap with the area investigated by Stoll et al. (2022), a fresh surface layer was prepared for LA-ICP-MS while the cryo-Raman analysis was performed 500 μm below the surface. Hence, an identical relative presence of specific minerals cannot be expected. In future comparisons, the approach based on chemical classification appears promising but will benefit from large sample populations of characterized dust particles, going alongside with a dedicated investigation of the spatial variability of the dust localization and geochemistry. Notably, the issue of spatial variability extends from the grain-scale (e.g., the heterogeneous population of impurities seen inside the grains here, Figures 4 and 6) to the scale of individual layers, such as an entire cloudy band, to the comparison of the variability inside different stratigraphic (e.g., annual) layers.
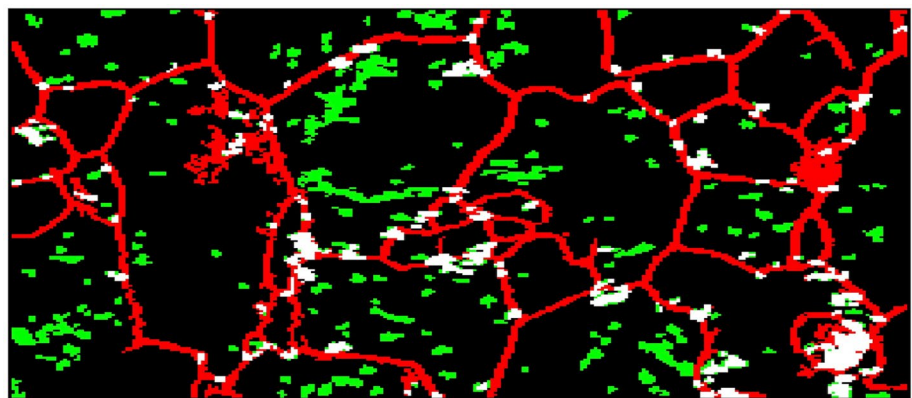
Figure 8. Example from Area 2 for a tentative differentiation of insoluble particle clusters located at grain boundaries (white) versus in the grain interior (green). Note that some misclassifications exist due to imperfect segmentation of the grain boundary network (see text).
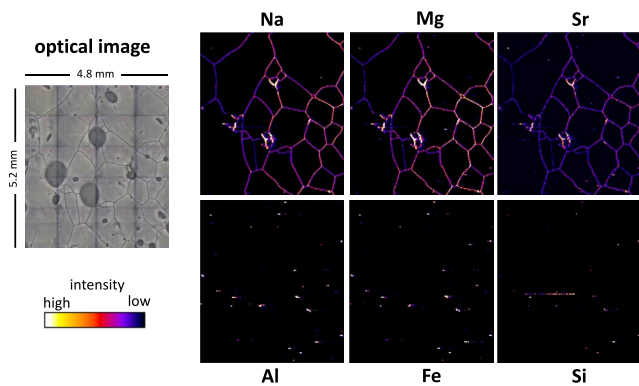
Figure 9. Comparison of the identical analytes as in the East Greenland Ice Core Project sample, here obtained in a sample from MIS2 in the EPICA Dome C ice core. Albeit not as abundant, dispersed bright spots are also visible, especially within Al, Fe and to a limited extent also in Si. The bright horizontal line in the lower half of the Si map is an artifact.

4.3. The Future of Chemical Imaging on Ice Cores With LA-ICP-MS

With respect to the initial development of LA-ICP-MS chemical imaging to ice cores (Bohleber et al., 2020) and the subsequent first application of the new technique to selected samples of Antarctic ice, the approach presented here represents an important improvement. The results show how adding new elements, first and foremost Al as a main element of terrestrial dust minerals, can open the investigation to the dust-related insoluble species, and reveal a refined picture of the glaciochemistry. Albeit requiring an about three-fold number of laser shots per map as compared to using a 35 μm spot, recording maps at 20 μm resolution proved to be essential to detect the dispersed bright spots, and to investigate their small-scale heterogeneity. Further increasing the spatial resolution to 10 μm and finer may help to map the heterogeneous chemical composition of the particle clusters at a finer scale but has to be weighed against an according increase in consumption of laser shots and instrumental resources. Having added the methodological improvements presented here, immediate future targets are additional "cloudy band" layers rich in insoluble impurities. In addition, it seems worthwhile to revisit Antarctic ice samples to investigate if evidence of clustered insoluble material is also found there. This would be of special interest for sections of Antarctic ice cores, where such particle aggregates have already been observed, comprising both shallow (Ellis et al., 2016) and deep sections (De Angelis et al., 2013; Lambert et al., 2008). Considering the much lower concentration of impurities in Antarctic ice in general, especially compared to the high dust content of the samples analyzed here, it may not be possible to include as many elements with one image recording, since larger dwell times may be required. This limitation could be overcome using a "time of flight" (TOF) mass spectrometer (Bohleber, Roman, Stoll, et al., 2021), offering to record a broad spectrum of elements in a single image acquisition. In this context, the additional maps shown in Figure 9 serve as a tentative reference for conditions in central Antarctica. These sections were obtained using a LA-ICP-TOFMS for imaging a sample of the last glacial period (MIS2) in the EPICA Dome C ice core, bag 1065. The maps were acquired using a 35 μm square spot, with 50% overlap between neighboring pixels to increase the spatial resolution horizontally. Further details on the experimental procedure have already been described elsewhere (Bohleber, Roman, Stoll, et al., 2021). Considering identical analytes as previously selected for the EGRIP samples, we find Na, Mg, and Sr to be strongly localized at grain boundaries, with only a few bright spots in the grain interiors. While showing comparatively more dispersed bright spots, the grain boundary association is absent for Al and Si, and only extremely weak for Fe. As a result, only few bright spots show spatial co-occurrence between these two groups of elements, in contrast to the EGRIP maps. Showing sufficient spatial co-occurrence, elemental ratios can be obtained for Mg/Na and Fe/Al following the identical approach to the EGRIP data (using a 95th percentile threshold), resulting in median values of 0.10 and 0.49, respectively (Figure S6 in Supporting Information S1). Si is not considered due to a weaker signal and an artifact (Figure 9). Notably, the Mg/Na values are closer to the bulk seawater ratio than the respective values obtained in the EGRIP YD samples, and the Fe/Al values are close to the upper continental crust values and the range reported for dust in the EDC core during the last glacial maximum (Marino et al., 2008). It is important to point out that one map alone permits drawing only very limited conclusions, and a direct comparison with reference values obtained from bulk meltwater sampling is greatly challenged by the unknown yet likely substantial amount of spatial variability in the ice. To this end, the EGRIP YD data sets show how several adjacent maps recorded with a 20 μm spot provide much refined detail. Yet, the EDC maps underline the principal transferability of the approach presented here, motivating future investigations of Antarctic ice. The broad spectrum of elements comprised in a LA-ICP-TOFMS data acquisition could also open the possibility to apply a more refined chemical classification scheme to the elemental maps, for example, adapting further what has been employed recently by Oyabu et al. (2020) for distinguishing particles related to dust and sea salt based on 7–8 elements. Based on the imaging afforded by LA-ICP-MS, image analysis techniques can be applied for selecting particle clusters that are located at, or in touch with, grain boundaries. Comparing the chemical signature, especially related to Fe, of particles at grain boundaries versus interiors could help to refine further the recently proposed view of deep ice as a "geochemical reactor," expecting post-depositional chemical reactions within the acidic environments of grain boundaries (Baccolo et al., 2021). In light of ongoing efforts to retrieve an "Oldest Ice Core" from Antarctica, it becomes clear that the special merit of the LA-ICP-MS technique goes beyond providing 1-D impurity profiles

at micron resolution. Especially if combined with other complementary techniques in a more holistic approach, chemical imaging with LA-ICP-MS may provide a key contribution to better understanding the impurity signals in deep ice, including elucidating the processes leading to particle cluster formation.

5. Conclusions

The present study has further refined the 2D chemical imaging on ice cores by LA-ICP-MS, through the exploration of analytes related to insoluble impurities and by increasing the spatial resolution to 20 μm. In contrast to the previously observed close association with the grain boundary network for Na, Mg, and Sr in Antarctic ice, maps obtained from a Greenland EGRIP and an Antarctic EPICA Dome C sample clearly show dispersed spot features at various locations in the grain interiors. Their average size and heterogenous chemical composition indicate that this image feature is related to clusters of insoluble material of various elements and sources. Based on a simple chemical classification on a pixel-by-pixel basis, it is possible to identify material of likely marine versus mineral dust origin. This interpretation is substantiated by elemental ratios being consistent with what is known about the respective aerosol sources. The extension of the LA-ICP-MS ice core imaging to specifically target insoluble particles opens the door for comparisons with other methods, such as single particle characterization from ice core meltwater and in particular cryo-Raman spectroscopy. A first evaluation of the maps that were obtained on the EGRIP sample previously analyzed by cryo-Raman spectroscopy shows that such an inter-method comparison provides considerable challenges but also indicates ways in which such a comparison may succeed. In concert with other techniques, chemical imaging with LA-ICP-MS is able to provide important complementary insight into the location of soluble and insoluble impurities in order to better understand their post-depositional change and interaction with the ice crystal matrix. Ultimately, this can deliver key insights in the preservation of impurity-related climate signals in the ice where it is needed the most: the deciphering of the deepest layers in a future "Oldest ice core."

Data Availability Statement

The underlying data used for creating the chemical maps in the study are available at zenodo.org via https://doi.org/10.5281/zenodo.7400718 with license Creative Commons Attribution 4.0 International.

References

Albani, S., Delmonte, B., Maggi, V., Baroni, C., Petit, J. R., Stenni, B., et al. (2012). Interpreting last glacial to Holocene dust changes at Talos Dome (East Antarctica): Implications for atmospheric variations from regional to hemispheric scales. *Climate of the Past*, *8*(2), 741–750. https://doi.org/10.5194/cp-8-741-2012

Baccolo, G., Delmonte, B., Albani, S., Baroni, C., Cibin, G., Frezzotti, M., et al. (2018). Regionalization of the atmospheric dust cycle on the periphery of the East Antarctic ice sheet since the last glacial maximum. *Geochemistry, Geophysics, Geosystems*, *19*(9), 3540–3554. https://doi.org/10.1029/2018GC007658

Baccolo, G., Delmonte, B., Di Stefano, E., Cibin, G., Crotti, I., Frezzotti, M., et al. (2021). Deep ice as a geochemical reactor: Insights from iron speciation and mineralogy of dust in the Talos Dome ice core (East Antarctica). *The Cryosphere*, *15*(10), 4807–4822. https://doi.org/10.5194/tc-15-4807-2021

Barnes, P. R. F., & Wolff, E. W. (2004). Distribution of soluble impurities in cold glacial ice. *Journal of Glaciology*, *50*(170), 311–324. https://doi.org/10.3189/172756504781829918

Barnes, P. R. F., Wolff, E. W., Mader, H. M., Udisti, R., Castellano, E., & Röthlisberger, R. (2003). Evolution of chemical peak shapes in the Dome C, Antarctica, ice core. *Journal of Geophysical Research*, *108*(D3), 4126. https://doi.org/10.1029/2002jd002538

Bohleber, P., Erhardt, T., Spaulding, N., Hoffmann, H., Fischer, H., & Mayewski, P. (2018). Temperature and mineral dust variability recorded in two low-accumulation Alpine ice cores over the last millennium. *Climate of the Past*, *14*(1), 21–37. https://doi.org/10.5194/cp-14-21-2018

Bohleber, P., Roman, M., Barbante, C., Vascon, S., Siddiqi, K., & Pelillo, M. (2021). Ice core science meets computer vision: Challenges and perspectives. *Frontiers of Computer Science*, *3*, 690276. https://doi.org/10.3389/fcomp.2021.690276

Bohleber, P., Roman, M., Šala, M., & Barbante, C. (2020). Imaging the impurity distribution in glacier ice cores with LA-ICP-MS. *Journal of Analytical Atomic Spectrometry*, *35*(10), 2204–2212. https://doi.org/10.1039/d0ja00170h

Bohleber, P., Roman, M., Šala, M., Delmonte, B., Stenni, B., & Barbante, C. (2021). Two-dimensional impurity imaging in deep Antarctic ice cores: Snapshots of three climatic periods and implications for high-resolution signal interpretation. *The Cryosphere*, *15*(7), 3523–3538. https://doi.org/10.5194/tc-15-3523-2021

Bohleber, P., Roman, M., Stoll, N., Busswiler, Y., & Rittner, M. (2021). Imaging the distribution of elements in Antarctic ice cores with LA-ICP-TOFMS. TOFWERK Application Note. Retrieved from https://www.tofwerk.com/imaging-ice-cores-la-icp-tofms/

Brook, E. J., Wolff, E., Dahl-Jensen, D., Fischer, H., Steig, E. J., & others (2006). The future of ice coring: International partnerships in ice core sciences (IPICS). *PAGES News*, *14*(1), 6–10. https://doi.org/10.22498/pages.14.1.6

De Angelis, M., Tison, J.-L., Morel-Fourcade, M.-C., & Susini, J. (2013). Micro-investigation of EPICA Dome C bottom ice: Evidence of long term in situ processes involving acid-salt interactions, mineral dust, and organic matter. *Quaternary Science Reviews*, *78*, 248–265. https://doi.org/10.1016/j.quascirev.2013.08.012

Della Lunga, D., Müller, W., Rasmussen, S. O., & Svensson, A. (2014). Location of cation impurities in NGRIP deep ice revealed by cryo-cell UV-laser-ablation ICPMS. *Journal of Glaciology*, *60*(223), 970–988. https://doi.org/10.3189/2014JoG13J199

Della Lunga, D., Müller, W., Rasmussen, S. O., Svensson, A., & Vallelonga, P. (2017). Calibrated cryo-cell UV-LA-ICPMS elemental concentrations from the NGRIP ice core reveal abrupt, sub-annual variability in dust across the GI-21.2 interstadial period. *The Cryosphere*, *11*(3), 1297–1309. https://doi.org/10.5194/tc-11-1297-2017

Eichler, J., Kleitz, I., Bayer-Giraldi, M., Jansen, D., Kipfstuhl, S., Shigeyama, W., et al. (2017). Location and distribution of micro-inclusions in the EDML and NEEM ice cores using optical microscopy and in situ Raman spectroscopy. *The Cryosphere*, *11*(3), 1075–1090. https://doi.org/10.5194/tc-11-1075-2017

Ellis, A., Edwards, R., Saunders, M., Chakrabarty, R. K., Subramanian, R., Timms, N. E., et al. (2016). Individual particle morphology, coatings, and impurities of black carbon aerosols in Antarctic ice and tropical rainfall. *Geophysical Research Letters*, *43*(22), 11–875. https://doi.org/10.1002/2016gl071042

Erhardt, T., Jensen, C. M., Borovinskaya, O., & Fischer, H. (2019). Single particle characterization and total elemental concentration measurements in polar ice using continuous flow analysis-inductively coupled plasma time-of-flight mass spectrometry. *Environmental Science & Technology*, *53*(22), 13275–13283. https://doi.org/10.1021/acs.est.9b03886

Faria, S. H., Freitag, J., & Kipfstuhl, S. (2010). Polar ice structure and the integrity of ice-core paleoclimate records. *Quaternary Science Reviews*, *29*(1–2), 338–351. https://doi.org/10.1016/j.quascirev.2009.10.016

Fischer, H., Blunier, T., & Mulvaney, R. (2021). Ice cores: Archive of the climate system. In *Glaciers and ice sheets in the climate system* (pp. 279–325). Springer.

Fischer, H., Severinghaus, J., Brook, E., Wolff, E., Albert, M., Alemany, O., et al. (2013). Where to find 1.5 million yr old ice for the IPICS" Oldest-Ice" ice core. *Climate of the Past*, *9*(6), 2489–2505. https://doi.org/10.5194/cp-9-2489-2013

Formenti, P., Schütz, L., Balkanski, Y., Desboeufs, K., Ebert, M., Kandler, K., et al. (2011). Recent progress in understanding physical and chemical properties of African and Asian mineral dust. *Atmospheric Chemistry and Physics*, *11*(16), 8231–8256. https://doi.org/10.5194/acp-11-8231-2011

Jeong, G. Y. (2008). Bulk and single-particle mineralogy of Asian dust and a comparison with its source soils. *Journal of Geophysical Research*, *113*(2), 1–16. https://doi.org/10.1029/2007JD008606

Jochum, K. P., Weis, U., Stoll, B., Kuzmin, D., Yang, Q., Raczek, I., et al. (2011). Determination of reference values for NIST SRM 610-617 glasses following ISO guidelines. *Geostandards and Geoanalytical Research*, *35*(4), 397–429. https://doi.org/10.1111/j.1751-908X.2011.00120.x

Khanal, A., & Estrada, R. (2020). Dynamic deep networks for Retinal vessel segmentation. *Frontiers in Computer Science*, *2*(August), 1–13. https://doi.org/10.3389/fcomp.2020.00035

Lambert, F., Delmonte, B., Petit, J. R., Bigler, M., Kaufmann, P. R., Hutterli, M. A., et al. (2008). Dust-climate couplings over the past 800,000 years from the EPICA Dome C ice core. *Nature*, *452*(7187), 616–619. https://doi.org/10.1038/nature06763

Lilien, D. A., Steinhage, D., Taylor, D., Parrenin, F., Ritz, C., Mulvaney, R., et al. (2021). Brief communication: New radar constraints support presence of ice older than 1.5, Myr at Little Dome C. *The Cryosphere*, *15*(4), 1881–1888. https://doi.org/10.5194/tc-15-1881-2021

Longerich, H. P., Jackson, S. E., & Günther, D. (1996). Laser ablation inductively coupled plasma mass spectrometric transient signal data acquisition and analyte concentration calculation. *Journal of Analytical Atomic Spectrometry*, *11*(9), 899–904. https://doi.org/10.1039/JA9961100899

Marino, F., Castellano, E., Ceccato, D., De Deckker, P., Delmonte, B., Ghermandi, G., et al. (2008). Defining the geochemical composition of the EPICA Dome C ice core dust during the last glacial-interglacial cycle. *Geochemistry, Geophysics, Geosystems*, *9*(10), Q10018. https://doi.org/10.1029/2008GC002023

McLennan, S. M. (2001). Relationships between the trace element composition of sedimentary rocks and upper continental crust. *Geochemistry, Geophysics, Geosystems*, *2*(4), 1021. https://doi.org/10.1029/2000gc000109

Mouri, H., Okada, K., & Shigehara, K. (1993). Variation of Mg, S, K and Ca contents in individual sea-salt particles. *Tellus B*, *45*(1), 80–85. https://doi.org/10.1034/j.1600-0889.1993.00007.x

Müller, W., Shelley, J. M. G., & Rasmussen, S. O. (2011). Direct chemical analysis of frozen ice cores by UV-laser ablation ICPMS. *Journal of Analytical Atomic Spectrometry*, *26*(12), 2391–2395. https://doi.org/10.1039/c1ja10242g

Ng, F. S. L. (2021). Pervasive diffusion of climate signals recorded in ice-vein ionic impurities. *The Cryosphere*, *15*(4), 1787–1810. https://doi.org/10.5194/tc-15-1787-2021

Oyabu, I., Iizuka, Y., Kawamura, K., Wolff, E., Severi, M., Ohgaito, R., et al. (2020). Compositions of dust and sea salts in the Dome C and Dome Fuji ice cores from Last Glacial Maximum to early Holocene based on ice-sublimation and single-particle measurements. *Journal of Geophysical Research: Atmospheres*, *125*(4), e2019JD032208. https://doi.org/10.1029/2019jd032208

Playà, E., & Rosell, L. (2005). The celestite problem in gypsum Sr geochemistry: An evaluation of purifying methods of gypsiferous samples. *Chemical Geology*, *221*(1–2), 102–116. https://doi.org/10.1016/j.chemgeo.2005.04.006

Rempel, A. W., Waddington, E. D., Wettlaufer, J. S., & Worster, M. G. (2001). Possible displacement of the climate signal in ancient ice by premelting and anomalous diffusion. *Nature*, *411*(6837), 568–571. https://doi.org/10.1038/35079043

Ruth, U., Wagenbach, D., Steffensen, J. P., & Bigler, M. (2003). Continuous record of microparticle concentration and size distribution in the central Greenland NGRIP ice core during the last glacial period. *Journal of Geophysical Research*, *108*(3), 1–12. https://doi.org/10.1029/2002jd002376

Sánchez-Román, M., McKenzie, J. A., de Luca Rebello Wagener, A., Romanek, C. S., Sánchez-Navas, A., & Vasconcelos, C. (2011). Experimentally determined biomediated Sr partition coefficient for dolomite: Significance and implication for natural dolomite. *Geochimica et Cosmochimica Acta*, *75*(3), 887–904. https://doi.org/10.1016/j.gca.2010.11.015

Sneed, S. B., Mayewski, P. A., Sayre, W. G., Handley, M. J., Kurbatov, A. V., Taylor, K. C., et al. (2015). New LA-ICP-MS cryocell and calibration technique for sub-millimeter analysis of ice cores. *Journal of Glaciology*, *61*(226), 233–242. https://doi.org/10.3189/2015jog14j139

Spaulding, N. E., Sneed, S. B., Handley, M. J., Bohleber, P., Kurbatov, A. V., Pearce, N. J., et al. (2017). A new multielement method for LA-ICP-MS data acquisition from glacier ice cores. *Environmental Science & Technology*, *51*(22), 13282–13287. https://doi.org/10.1021/acs.est.7b03950

Stoll, N., Eichler, J., Hörhold, M., Erhardt, T., Jensen, C., & Weikusat, I. (2021). Microstructure, micro-inclusions, and mineralogy along the EGRIP ice core–Part 1: Localisation of inclusions and deformation patterns. *The Cryosphere*, *15*(12), 5717–5737. https://doi.org/10.5194/tc-15-5717-2021

Stoll, N., Eichler, J., Hörhold, M., Shigeyama, W., & Weikusat, I. (2021). A review of the microstructural location of impurities in polar ice and their impacts on deformation. *Frontiers in Earth Science*, *8*, 658. https://doi.org/10.3389/feart.2020.615613

Stoll, N., Hörhold, M., Erhardt, T., Eichler, J., Jensen, C., & Weikusat, I. (2022). Microstructure, micro-inclusions, and mineralogy along the EGRIP (East Greenland ice core project) ice core–Part 2: Implications for palaeo-mineralogy. *The Cryosphere*, *16*(2), 667–688. https://doi.org/10.5194/tc-16-667-2022

Svensson, A., Nielsen, S. W., Kipfstuhl, S., Johnsen, S. J., Steffensen, J. P., Bigler, M., et al. (2005). Visual stratigraphy of the North Greenland Ice Core Project (NorthGRIP) ice core during the last glacial period. *Journal of Geophysical Research*, *110*(D2), D02108. https://doi.org/10.1029/2004jd005134